Harnessing Stratospheric Diffusion Barriers for Enhanced Climate Geoengineering

Nikolas O. Aksamit[1], Ben Kravitz[2,3], Douglas G. MacMartin[4], George Haller[1]

[1]Institute for Mechanical Systems, Swiss Federal Institute of Technology (ETH), Zürich, Switzerland.
[2]Department of Earth and Atmospheric Sciences, Indiana University, Bloomington, IN, USA.
[3]Atmospheric Sciences and Global Change Division, Pacific Northwest National Laboratory, Richland, WA, USA.
[4]Sibley School of Mechanical and Aerospace Engineering, Cornell University, Ithaca, NY, USA.

Correspondence to: Nikolas O. Aksamit (naksamit@ethz.ch)

Abstract. Stratospheric sulfate-aerosol geoengineering is a proposed method to temporarily intervene in the climate system to increase reflectance of shortwave radiation and reduce mean global temperature. In previous climate modeling studies, choosing injection locations for geoengineering aerosols has thus far only utilized average dynamics of stratospheric wind fields instead of accounting for the essential role of time-varying material transport barriers in turbulent atmospheric flows. Here we conduct the first analysis of sulfate aerosol dispersion in the stratosphere comparing a now-standard fixed-injection scheme with time-varying injection locations that harness short-term stratospheric diffusion barriers. We show how diffusive transport barriers can quickly be identified and inform optimal injection locations using short forecast and reanalysis data. Within the first seven days of transport, the dynamics-based approach is able to produce particle distributions with greater global coverage than fixed-site methods with fewer injections. Additionally, this enhanced dispersion slows aerosol microphysical growth, increasing lifespan of sulfate aerosols at monthly and yearly timescales. We conclude that previous feasibility studies of geoengineering likely underestimate the cooling efficiency of sulfate aerosol geoengineering.

1 Introduction

Stratospheric sulfate-aerosol geoengineering relies on triggering an atmospheric perturbation through deliberate injections of sulfate aerosol precursors (often SO_2) into the lower stratosphere to mimic the cooling effects seen after large volcanic eruptions [The Royal Society, 2009]. Over the last several decades, this has been suggested as a possible means of reducing some of the impacts of climate change [e.g., Crutzen, 2006]. There are, however, many open questions about the effects of radiative forcing from sulfate injections [Kravitz and MacMartin, 2020]. The importance of choosing the altitude and latitudes of injection, and distribution of injection rates across those, has been clearly demonstrated, as well as adjusting the seasons of injection [cite]. Additionally, even for sulfate aerosol, the method of dispersal will affect aerosol size distribution, and hence the amount of material that needs to be injected. To date, many of these uncertainties are based on a climate response from fixed-injection locations [e.g. Robock et al., 2008; Heckendorn et al., 2009; Tilmes et al., 2017], a significant limitation for predicting dispersion in time-varying flows. In fact, none of these studies consider the short-term variations of stratospheric

winds or the organizing role of turbulent coherent structures in these time-varying flows. Driscoll et al. [2012], however, showed that it is impossible to correctly capture the impact of abrupt atmospheric perturbations on surface climate without a well-resolved stratospheric model. With the great significance of stratospheric dynamics for teleconnections and the state of the atmosphere [e.g. Jaiser et al., 2013, Domeisen et al., 2018], how can we optimize where to put aerosols or precursors so that we have greater influence on the mean climate, and with better efficiency?

While benchmark studies have been quite successful at understanding the mean climatic response of geoengineering in sophisticated Earth System Models [e.g. Kashimura et al., 2017; Kravitz et al., 2017], the injection protocols have all neglected presently-available short-term predictive information useful for optimizing particle dispersion. An efficient dispersion of aerosol precursors is of crucial importance for aerosol coagulation [Kravitz and MacMartin, 2020]: the particle size distribution is a critical and sensitive parameter for accurately determining surface cooling, stratospheric warming, and changes in stratospheric dynamics [e.g., Rasch et al., 2008; Heckendorn et al., 2009; Tilmes et al., 2008; Niemeier et al., 2011]. By only considering mean flow, one limits geoengineering evaluations to simple injection protocols that do not fully exploit turbulence coherence or mixing in the stratosphere. This increases the likelihood of a heterogeneous spatial coverage and localized high concentrations of aerosols, leading to enhanced coagulation and sedimentation rates [e.g., Pierce et al., 2010]. Without a more precise optimization of injection locations, we limit our ability to accurately model full potential impacts of geoengineering.
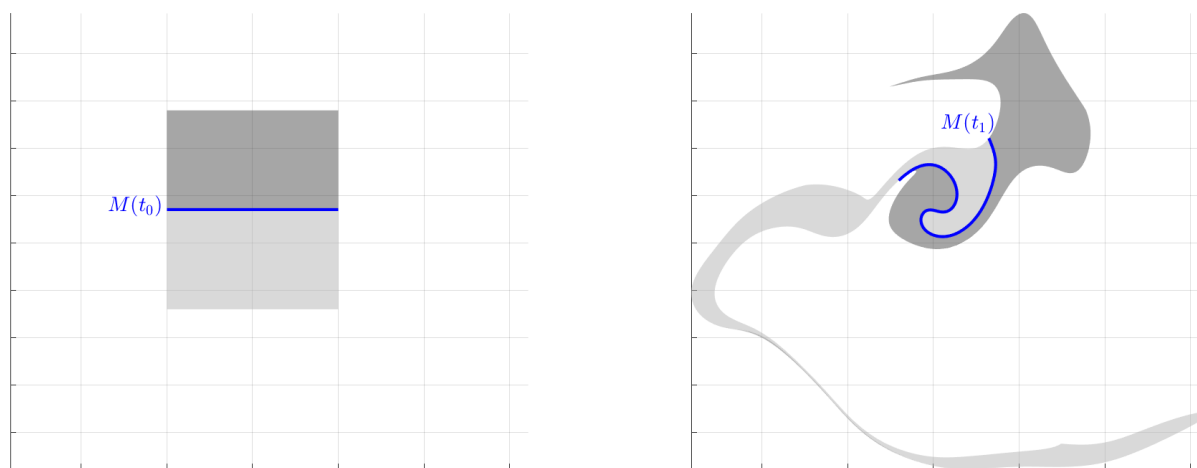
Figure 1: Example of fluid particle advection for an unsteady geophysical 2D fluid flow from time t_0 to time t_1. For any arbitrary line of initial fluid particle positions, such as $M(t_0)$, that line will be a barrier to advective transport and mixing. This is seen in the second panel as no dark grey fluid has crossed $M(t_1)$ to mix with the light grey fluid.

Instead of standard fixed-locations, we propose a time-varying injection location protocol based on identification and prediction of short-term Lagrangian stratospheric transport barriers. This method harnesses the theory of Lagrangian coherent

structures (LCSs), a tool for highlighting the most influential material surfaces solely from fluid velocity fields without any further modeling of scalar transport [Haller, 2015]. For a given unsteady fluid flow, any arbitrary surface of fluid particles, M, will block advective transport across that surface over time as the surface deforms with the flow. This is shown in a 2D velocity field of geostrophic ocean surface currents in Figure 1. Here, the blue line M separates regions of light and dark grey fluid particles. As the fluid flows from time t_0 to t_1, M is an advective transport barrier in that no dark grey fluid crosses M to mix with the light grey fluid. This result follows immediately from the continuity of the equations defining fluid motion.

Instead of looking for material barriers to advective transport, of which there are infinitely many, LCS theory identifies only exceptional distinguished material surfaces, such as those that are mathematically defined to be rotationally coherent, undergo minimal stretching over time, or locally attract or repel nearby fluid particles at a significant rate. One example of the latter two structures, termed hyperbolic LCS, and their time evolution in the same unsteady ocean flow are shown in Figure 4. Over the time period t_0 to t_2, M_A is the structure that is mathematically-defined to most effectively attract nearby particles, and M_R repels nearby particles. By identifying exceptional material barriers, such as the saddle feature in Figure 2, LCS theory allows organization of turbulent fluid flows into coherent patterns in a mathematically-rigorous (non-empirical), physical and frame-independent manner [Haller, 2015].
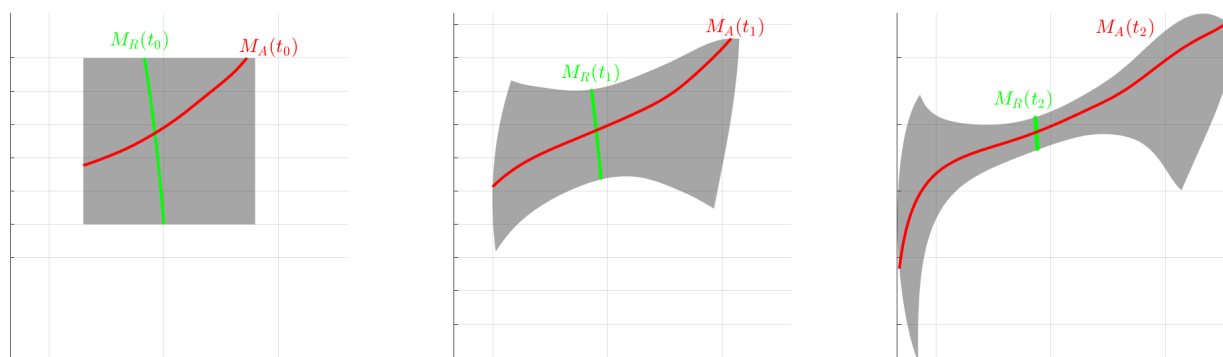
Figure 2: Example of time evolution of fluid particles surrounding hyperbolic LCS in a geophysical fluid flow from time t_0 to t_2. M_A is an attracting LCS (unstable-manifold) and M_R is a repelling LCS (stable-manifold).

Though the mathematical definition of atmospheric flow structures as LCS is restrictive, LCS have actually been identified throughout the atmosphere [Tang et al., 2010; Tallapragada et al., 2011; Rutherford et al., 2012; BozorgMagham and Ross, 2015; Knutson et al., 2015; Wang et al., 2017]. Of particular relevance to the present research is the LCS work of Beron-Vera et al. [2012] who demonstrated how zonal jets behave as meridional transport barriers at high latitudes. Olascoaga et al. [2012] analyzed LCS in stratospheric winds to provide a rigorous definition of the transport barriers contributing to the loss of ozone from the Arctic ozone layer, and there was recent success in delineating LCS along atmospheric rivers [Garaboa-Paz et al., 2015]. Jupiter's Great Red Spot and zonal jets were identified as material transport barriers through video analysis and LCS

theory [Hadjighasem and Haller 2016]. Using a null-geodesic identification scheme, the northern polar vortex, a significant

80 structure in high-latitude atmospheric mixing, was accurately identified as a transport-blocking LCS [Serra et al., 2017]. Lastly, Wang et al. [2017] were able to use a related diagnostic strain-tensor field to predict the location of space shuttle contaminant plumes in the thermosphere after 48 hours of transport. These previous results indicate the potential for the most influential LCS to be harnessed for geoengineering purposes. Specifically, hyperbolic LCS that maximize or minimize dispersion may be used as time-varying injection locations that reduce coagulation of aerosols and increase their lifespan and

85 utility.

Recently, Haller et al. [2018, 2020] derived an additional objective criterion that specifically identifies the strongest barriers and enhancers of diffusive particle transport. That is, moving material barriers in a fluid flow that maximize or minimize the diffusive contribution in the advection-diffusion equations over a given timeframe. They have obtained a diffusion barrier strength (DBS) field whose ridges highlight the strongest diffusive transport barriers in forward-time analysis and strongest

90 diffusive transport enhancers in backward-time analysis, without actually modeling the evolution of a diffusive scalar field. For atmospheric science, this significantly reduces the computational burden for predicting how scalar fields will evolve as it provides quantitative information about future attraction and dispersion patterns without needing complex numerical machinery to model the advection-diffusion equations, or making assumptions about their unknown initial- and boundary conditions. In comparison, the effective-diffusivity approach of Nakamura [2008] provides an a posteriori visualization of

95 Eulerian barriers, but only after scalar transport simulations have been performed. DBS fields, however, give an a priori (predictive) characterization of material barriers to diffusion without ever running diffusive simulations. This new technique increases the rigor of Lagrangian atmospheric analysis and removes ambiguity arising from the lack of a universal definition of coherence in atmospheric LCS work. As such, the DBS field is perfectly suited for optimizing aerosol dispersion and is computable solely from available wind fields forecasts and hindcasts or reanalysis.

100 In this manuscript, we evaluate simulated stratospheric flows with the aim of identifying diffusive transport barriers and informing injection site selection for enhanced stratospheric geoengineering via aerosols. In doing so, we provide an initial demonstration of the benefits of incorporating atmospheric dynamics into geoengineering analyses and provide suggestions to better assess its potential impacts. Our choice of dynamics-informed injections is evaluated against fixed-injection protocols via long-term metrics of pure advective transport, and for geoengineering scenarios simulated in a fully coupled climate-model.

105 We find significant improvement in the ability of injected aerosols to achieve geoengineering objectives over the standard methods. We then introduce further practical and logistical restrictions on the DBS-based protocol, and maintain our method's improved performance.

2 Methods

2.1 Climate Model Data

110   We use CESM2 (WACCM6) [Gettelman et al., 2019] under an SSP5-8.5 scenario to generate global wind fields at 72 levels for 18.75 years of simulation. These fields were computed at a spatial resolution of 0.94° latitude and 1.25° longitude, with instantaneous output at 6-hour frequency. As vertical motion is minimized over short timescales along isentropic surfaces, and similar analysis has reliably identified transport barriers on these surfaces [Serra et al., 2017], we extracted wind fields along isentropes ranging from T=280 K to 1000 K with 20 K resolution. This is expected to provide a computationally efficient 2D

115   analysis of material barriers to particle transport. We primarily focus on the T=540 K isentrope in the lower stratosphere (approximately 20-25 km ASL in the tropics) as these elevations are at the upper limit of currently practical aerosol injection heights. The fundamental differences we find between the DBS-injection and fixed-injection protocols are, however, relevant for any height.

A preliminary dispersion analysis was first conducted by modeling aerosols as non-reactive fluid-particles. At the beginning

120   of each month for the full 18.75 years of CESM2 (WACCM6) model simulation, injection locations were defined using a short temporal neighborhood of the wind-field output from CESM2 (WACCM6). The advection of dense parcels of fluid particles from neighborhoods surrounding those injection points was then computed for the next week. This approximation of aerosol transport by perfectly fluid-following particles inherently assumes that there are negligible inertial effects and the aerosol vertical motion is not influenced by radiative heating or cooling of the particle. While these assumptions limit any study of

125   climate impacts, these calculations provide a longitudinal study of dynamics-informed injection dispersion spanning numerous natural climate cycles and allows comparison with traditional injection protocols.

We complement our basic fluid-particle trajectory analysis with a comprehensive CESM2 (WACCM6) simulation suite of one-year simulations with sulfate precursor injections occurring during each season. These simulations incorporate the advection of aerosols with full microphysics, atmospheric chemistry and radiative forcing components, with all other earth

130   system model components. Again, the performance of DBS-informed and fixed-location sites are compared. As the inclusion of microphysics and atmospheric chemistry makes these simulations computationally more expensive, the subsequent evolution of each injection is only computed for one calendar year after injection.

2.2 Lagrangian transport extremizers

135   Diffusion Barrier Strength (DBS) is an objective (i.e. observer-independent) diagnostic field whose ridges highlight diffusive or stochastic transport extremizers from velocity data [Haller et al., 2018]. For a given time-varying velocity field $\mathbf{v}(\mathbf{x}, t)$, and tracer $c(\mathbf{x}, t)$ we can describe the evolution of this tracer with the classic advection-diffusion equation:

$$\frac{\partial c}{\partial t} + \nabla \cdot (c\mathbf{v}) = \nu \nabla \cdot (\mathbf{D}\nabla c), \quad c(x, t_0) = c_0(x),$$

where $\mathbf{D}(\mathbf{x}, t)$ is the symmetric, positive definite diffusion-structure tensor. The left-hand-side of this differential equation
140   contains the advection of this scalar field whereas the right-hand-side describes transport due to diffusive processes.
Furthermore, we define the path of a fluid particle in the velocity field $\mathbf{v}(\mathbf{x}, t)$ as a solution to the ordinary differential equation
$\dot{\mathbf{x}} = \mathbf{v}(\mathbf{x}, t)$, described by the flow map:

$$\mathbf{F}_{t_0}^t(\mathbf{x_0}) = \mathbf{x}(t, t_0, \mathbf{x_0}).$$

From here, we define the DBS at a point $\boldsymbol{x_0}$ over the time interval $[t_0, t_1]$ as

145
$$DBS(\mathbf{x_0}) = \text{trace } \overline{\mathbf{T}}_{t_0}^{t_1}(\mathbf{x_0}),$$

where   overbar   denotes   the   time-average   of   the   transport   tensor
$\mathbf{T}_{t_0}^{t_1}(\boldsymbol{x_0}) = \left[\nabla \mathbf{F}_{t_0}^t\right]^{-1} \mathbf{D}(\nabla \mathbf{F}_{t_0}^t, t) \left[\nabla \mathbf{F}_{t_0}^t\right]^{-\intercal}$, over $[t_0, t_1]$.

The diffusion-structure tensor $\mathbf{D}$ is capable of representing parameterizations of many complex diffusion-like processes, but
our research focuses on molecular (i.e. homogeneous, isotropic and steady) diffusion, in which case $\mathbf{D}(\mathbf{x}, t)$ is constantly the
150   identity matrix. In this situation, the transport tensor $\mathbf{T}_{t_0}^{t_1}$ reduces to the inverse of the Cauchy-Green strain tensor, $\mathbf{C}_{t_0}^{t_1} = \left[\nabla \mathbf{F}_{t_0}^t\right]^{\intercal} \nabla \mathbf{F}_{t_0}^t$, that also arises in the computation of the Finite-Time Lyapunov Exponent (FTLE) used in previous atmospheric
transport barrier studies [see, e.g., Beron-Vera et al., 2012; Olascoaga et al., 2012; Garaboa-Paz et al., 2015; Serra et al., 2017;
Wang et al., 2017]. DBS values are, therefore, pointwise equal to the trace of the time-averaged $[\mathbf{C}_{t_0}^{t_1}]^{-1} = \left[\nabla \mathbf{F}_{t_0}^t\right]^{-1} \left[\nabla \mathbf{F}_{t_0}^t\right]^{-\intercal}$
tensor. One notable difference between DBS and FTLE is the inclusion of diffusive or stochastic transport in the definition of
155   transport barriers or enhancers for DBS, a process essential to predicting aerosol dispersion in the stratosphere. The inclusion
of diffusion in the transport functional allows for a systematic search for extremizing surfaces to transport [Haller et al., 2018],
thereby eliminating the ambiguity inherent in various available coherent structure definitions [see Haller, 2015]. Accounting
for diffusive and stochastic transport necessarily leads to the inclusion of $\mathbf{C}_{t_0}^t$ tensors for all $t \in [t_0, t_1]$ in the definition of the
DBS. In contrast, computing the FTLE only includes the single tensor $\mathbf{C}_{t_0}^{t_1}$.

160   Using a limited time-window of the modelled wind flow for DBS calculations, we were able to effectively simulate a real-time
geoengineering scenario. At the beginning of each month during our 18.75 years of simulation, we analyzed one week of future
flow data and one week of previous flow data as proxies for forecast and reanalysis, respectively, to determine optimal locations
for sulfate injection. That is, on a given day t_0, the one-week DBSFW field was calculated from t_0 to $t_0 + 7$, and under reversal
of the direction of the flow in the reanalysis data, the DBSBW field was calculated from t_0 to $t_0 - 7$. As is described by Haller
165   et al. [2018], the ridges of DBSFW highlight locations of strongest dispersion (i.e. diffusive transport limiters) on the globe at
t_0, while the ridges of DBSBW indicate the locations of the strongest accumulation (i.e. diffusive transport enhancers) at t_0.
These diffusive transport barriers are analogous to the structures M_A and M_R from Figure 2, but account for diffusive as well

as advective transport in the flow. To identify DBS ridges, we advected fluid particles along isentropic surfaces to simplify
calculations and ignored vertical motions.
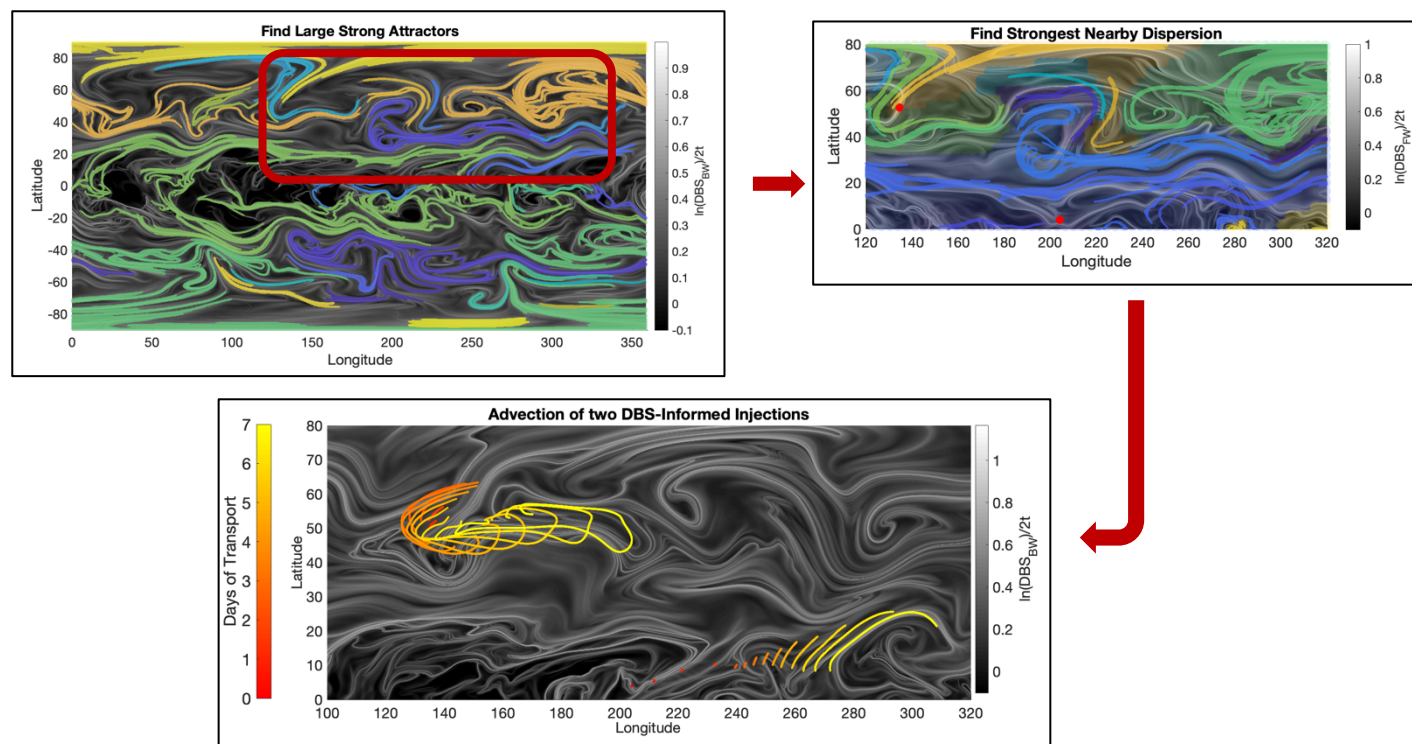
**Figure 3: Example flow chart of DBS-informed injection scheme from 360K to highlight the selection process for a
more complex flow. Clockwise from top left: Calculate seven-day DBS$_{BW}$ field and identify strongly attracting
connected flow-structures above a certain threshold; Identify the points closest to each attracting structure and choose
a unique strongest seven-day DBS$_{FW}$ (repelling) point for each attracting structure; injecting aerosols at these points
will cause them to spread quickly and converge to dominant attracting structures.**

We identified strongly attracting flow features as connected components of the DBS$_{BW}$ field with values above a simple fixed
threshold. This threshold was chosen empirically from the range of DBS values in these calculations and was constant for all
structure identification at all t_0. As seen also for other objective coherent structures identified from short-term calculations
[e.g., Serra and Haller, 2016], these seven-day attracting features persist for much longer than their domain of computation in
the flow and attract many nearby fluid particles. Near each strongly attracting feature, the location with the largest DBS$_{FW}$
value signals a potential injection site for geoengineering as it indicates the strongest local dispersion over the next seven days.
We balance strong dispersion and nearby strong attractors to both maximize spread of aerosols and prevent multiple injections
being attracted to the same regions. When possible, this methodology prevented aerosols injected at initially distant sites from
traveling great distances only to be attracted to the same portion of the flow. A flow chart detailing the injection-location
selection process is shown in Figure 3.

While we prioritize injecting near unique attractors, this was not always possible given that single DBS_{BW} ridges could also span much of the globe. Thus, we also allowed seeding near separate regions of the same attractor. If seven separate attractors are not available at a given time, we simplify the process and choose the maximal DBS_{FW} site in each of seven latitude bands: [-7.5°, 7.5°], [±7.5°, ±22.5°], [±22.5°, ±37.5°], [± 37.5°, ±62.5°]. The dynamics-based approach introduced here adapts to any isentrope or future climate scenario as the injection location choice always depends on the current state of the stratosphere at injection time.
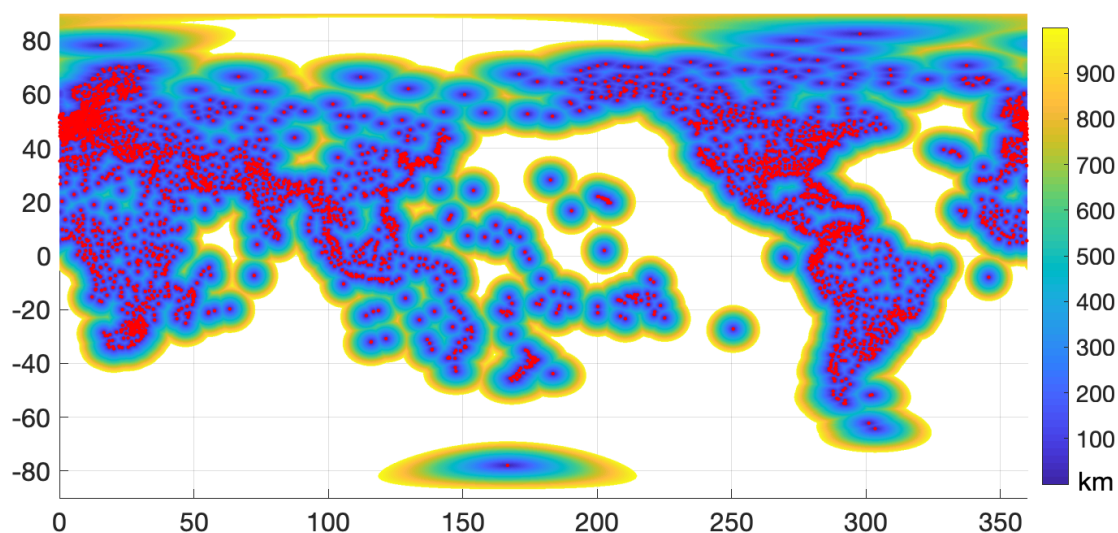
Figure 4: Global coverage of potential injection locations for an airport-bound scenario including a map of 9300 airport locations (red dots) and the distance to the nearest airport up to 1000 km.

We compared our DBS injection scheme to a baseline scheme that injected sulfate aerosols at seven fixed-injection locations $(0, \pm15, \pm30$ and $\pm50°$ latitude at 260° longitude) similar to those explored by others [e.g. Robock et al., 2008; Heckendorn et al, 2009; Tilmes et al., 2017]. Lastly, we ran a scenario where the DBS-injection site had to be within 1000 km of an airport [Global Airport Database, 2020] as a logistical handicap more similar to real world possibilities (Figure 4). For both the unrestricted DBS and the airport protocols, we limited the selection of injection locations to latitudes between ±62.5° to avoid trapping by meridional barriers near the poles [Beron-Vera et al., 2012] and maximize global coverage. Despite this restriction, the stratospheric flow is still able to mix particles to higher latitudes (Figures 3 and 5).

2.3 Geoengineering performance metrics

For our basic dispersion analysis, we evaluated the effective global coverage and rate of dispersion via an average minimum-
205 distance metric defined as

$$\mu(t) = \frac{1}{N} \sum_{\boldsymbol{x} \in D} \min\left(d(\boldsymbol{x}, \gamma(t))\right), \tag{1}$$

where $\boldsymbol{x} \in D$ are all points on the globe, d is the great-circle distance, $\gamma(t)$ is the location of all aerosols at time t, and N is the number of grid points on the globe used for the calculation. Lower values of μ indicate a shorter distance from any point on the globe to the nearest aerosol, and thus imply better coverage. As volumetric or mass concentrations of aerosols are driving factors in many of the microphysical processes governing aerosol lifespan, we also calculated the entropy of the distribution
210 of aerosol concentrations p_k in discretized bins

$$E = -\sum_{\boldsymbol{x} \in D} p_k \log_2\left(\frac{p_k}{w_k}\right), \tag{2}$$

where w_k is the size of a bin [Harris, 2006]. The evolution of the entropy of each injection protocol was normalized by the entropy of a perfectly uniform distribution of aerosols to give a relative entropy value.

We compared the cumulative coverage of injections using seven DBS-informed locations (with and without airport restrictions) and seven fixed-locations for up to 50 weeks of advection over the entire 18.75-year simulation period. In this
215 initial experiment, we did not inject aerosols into CESM2(WACCM6), but computed advection of fluid particles in wind fields generated by CESM2(WACCM6).

In our second experiment, we used precomputed wind fields to determine injection sites, and then recomputed a fully-coupled microphysics simulations, where the atmosphere was influenced by geoengineering. The effective global coverage, increase in airborne H2SO4 mass, and the lifespan of the aerosols was then compared for the three injection protocols. The effective
220 lifespan was calculated as the first instance at which the atmospheric H2SO4 load dropped below the total mass prior to injection.

3 Results

3.1 DBS influence on aerosol dispersion

225 For the advection simulation without microphysics, the global coverage of aerosols injected at seven dynamically varying (DBS-informed) injection locations was much greater than coverage from the seven fixed-injection locations. We found an immediate increase in global coverage for the DBS-informed injections, as predicted from the mathematical definition of large DBS_{FW} values. Figures 5a and 5c detail how the zonal concentrations of ideal sulfates injected at the standard fixed-locations evolve over the first seven days of transport during boreal Summer and Winter, respectively. While there is North-South movement of the volume of particles, there is little-to-no dispersion by the end of the first week. This visualization is

230 complemented by the time evolution and minimal change of relative entropy during the same time period in the bottom two subplots of Figure 5.
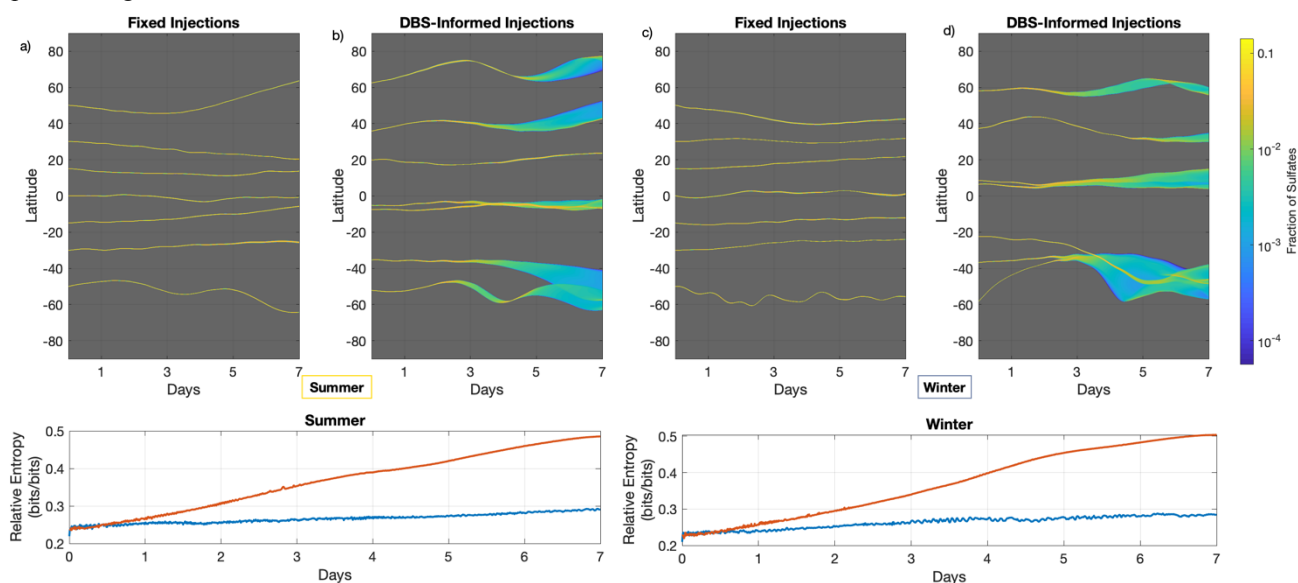
Figure 5: DBS-informed injection yields significantly enhanced coverage over fixed-location injections over short-term, seven-day periods. Zonal concentrations during one week of aerosol transport using the two injection protocols are displayed in subplots a-d with their respective relative entropy values in the lower subplots.

235

In contrast, by the third day of transport, Figure 5b and 5d show that the DBS-informed injections have begun efficiently spreading and increasing global coverage. As is discussed later and shown in the full microphysics simulations in the next section, this has an implicit impact on the rate of coagulation, sedimentation, and the lifespan of the aerosols. By the end of the first seven days, the DBS-informed injection has covered a large portion of the northern and southern hemispheres from

240 −70° to 70° for both the Summer and Winter injections. This difference in global coverage is further quantified by the relative entropy of aerosol distributions for the two protocols. In the bottom two subplots of Figure 5, the aerosol distribution from the DBS injections has greater entropy (Eq. 2) beginning on the first day of transport and increasing in performance through the end of the week. At the same time, the near constant entropy for the fixed-locations verifies that the initial injection parcels

have not dispersed, and hence potentially increase "hot-spotting" in the stratosphere and contribute to less uniform radiative

245   forcing.
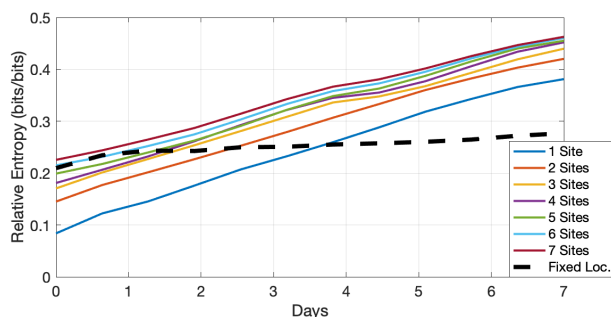
Figure 6: Relative entropy of DBS-informed injections under a varying number of sites for the summer simulation in Figure 5. Through optimizing injections near dispersion enhancing transport barriers, we are able to achieve significantly more uniform distributions of aerosols with fewer necessary injection sites.

250
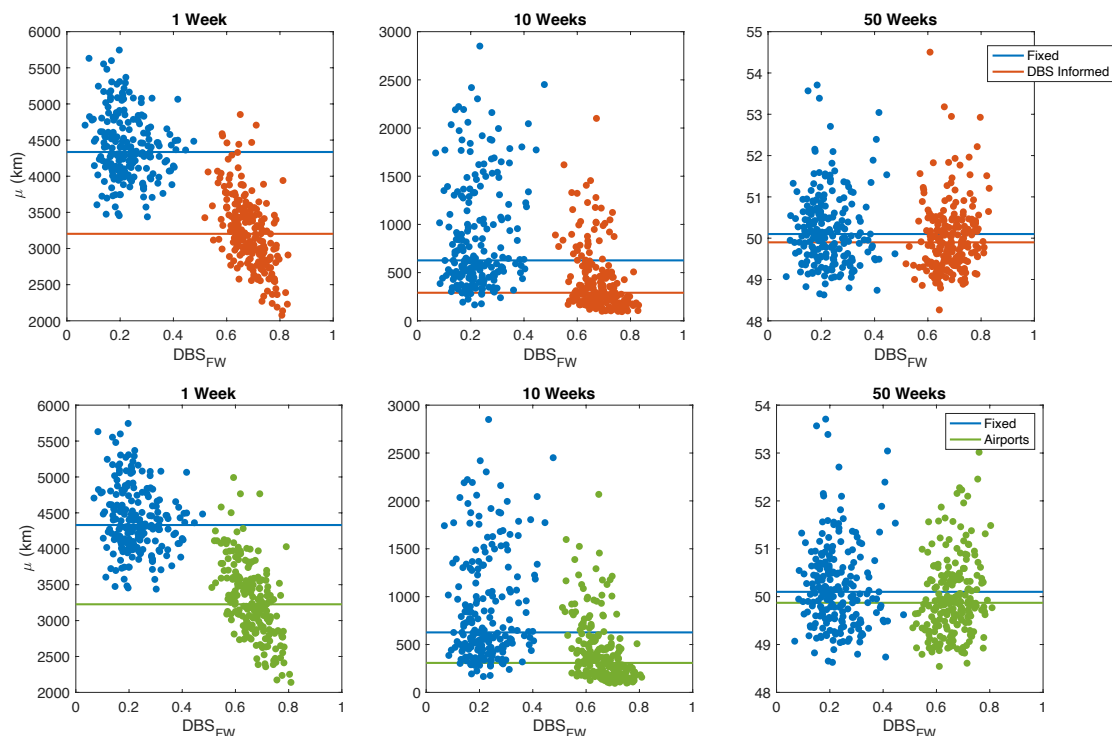
Figure 7**: Average distance to nearest aerosol (Eq. 1) with injections initialized each month for 18.75 years. The top three subplots compare the fixed location protocol to the DBS informed injection after 1 week, 10 weeks and 50 weeks of transport, with cluster means marked by respective horizontal lines. The bottom three subplots are analogous with the added restriction that DBS informed injections must also be within 1000 km of an airport. Both DBS approaches**

255   **outperform the fixed injections protocols up to 10 weeks, suggesting flexibility of the protocols and utility of harnessing Lagrangian coherent structures for enhancing dispersion.**

The enhanced dispersion, made possible by harnessing DBS information, also allows for a simplification of injection operations. Using the same time period from Figure 5a-b, we were able to leverage the enhanced concentration distributions and test how reducing the number of DBS injection sites would influence the subsequent aerosol coverage. Figure 6 shows that for one such test, almost immediately, there is a negligible reduction in relative entropy when reducing from seven DBS-informed injections to six. That is, within the first day of dispersion, a near 15% reduction in injected material and injection sites does not reduce the performance of our DBS protocol to levels below that of the fixed locations. After three days, when the influence of strong DBS barriers have been more effective, reducing injection to only two DBS-informed locations still resulted in a more uniform concentration distribution than the seven fixed locations. After four days, a single injection site was dispersing aerosols in the stratosphere more effectively than the combination of seven fixed sites. The advantages of a well-informed injection location could thus provide significant benefit to reduce hot-spotting and heterogeneous radiative forcing, as well as reduce the economic burden of a geoengineering program.

To determine if DBS-informed injections would consistently increase dispersion over all seasons, and over many years, we consider the cumulative statistics of many long-term advection models. At monthly intervals, the same seven-day reanalysis and forecast method was used to choose DBS-injections locations, both with and without a 1000 km distance restriction to the nearest airport. After 1 week, 10 weeks, and 50 weeks of transport, μ values (Eq. 1) were computed and compared to the fixed-injection protocol. Figure 7 shows the results of this experiment for transport periods spanning the whole 18.75 years. Clusters of μ values indicate variance in the response of aerosol transport to different DBS ridge structures over time, but mean values of those clusters (indicated by horizontal lines) consistently show improved coverage compared to the fixed protocol. As noted before, the most considerable enhancement in dispersion was seen immediately, supporting a probable influence on aerosol microphysics during the first week of transport. After 10 weeks, DBS-informed injections were still more effective at global coverage than the fixed-location protocol, even with the airport restrictions, but at yearly timescales, the average improvement was minimal. It should be noted that the variance of global coverage was also lowest for DBS-informed seeding at 10 and 50 weeks.

3.2 Full atmospheric chemistry and microphysics simulations

Beyond improved advective transport of aerosols, we also wish to investigate the role that diffusion transport barriers may play in dampening microphysical processes that can reduce the lifespan of geoengineering aerosols, such as coagulation and sedimentation, in a fully coupled climate model. To address this, we selected the DBS-informed and airport-restricted DBS-informed location selection methods at the beginning of four months (January, April, July, September) from one year of CESM2 (WACCM6) output. For each t_0 we reran the CESM2 (WACCM6) model from t_0 forward for the three separate protocols after injecting 10 Tg of SO₂ on a single day, spread evenly across the seven injection sites on the 540 K isentrope. This resulted in twelve year-long model simulations that calculate the total evolution of injections from each geoengineering protocol. The mol/mol concentrations of H_2SO_4 was measured on nineteen isentropes spanning 360 to 720 K.

290   The first notable finding is the increase in the lifespan of the aerosols for the DBS-informed and airport-restricted injection
protocols. Each subplot in Figure 8 details the evolution of the total mass of the modeled H_2SO_4 in the atmosphere, as compared
to pre-injection values, for one year. The date at which the H_2SO_4 mass returned to within 10% of pre-injection values is
marked for each protocol with a vertical dashed line. For each of the four seasons of injection, the two DBS-informed protocols
enhanced the lifespan of aerosols and increased the impact of geoengineering as compared to the standard fixed-location

295   approach. The largest increases in lifespan, those from injections in April, were evenly split for the Northern and Southern
hemispheres. The second largest increase in lifespan (October injections) was largely caused by prolonged transport in the
Southern hemisphere. On average these improvements resulted in a 22.5 day increase in the lifespan of aerosols for the
unrestricted DBS-informed method and a 24.5 day increase in lifespan for injections with the 1000 km airport restriction. The
extended lifespan after imposing the airport restriction is due to the chaotic three-dimensional nature of atmospheric flows and

300   influence of longtime flow evolution that is unknown for the seven-day isentrope-restricted DBS calculations. Spikes in H_2SO_4
mass that occur after the initial injection peak are the result of the vertical transport of modeled aerosols moving back into the
measurement domain, e.g., crossing the 360 K or 720 K isentropes.
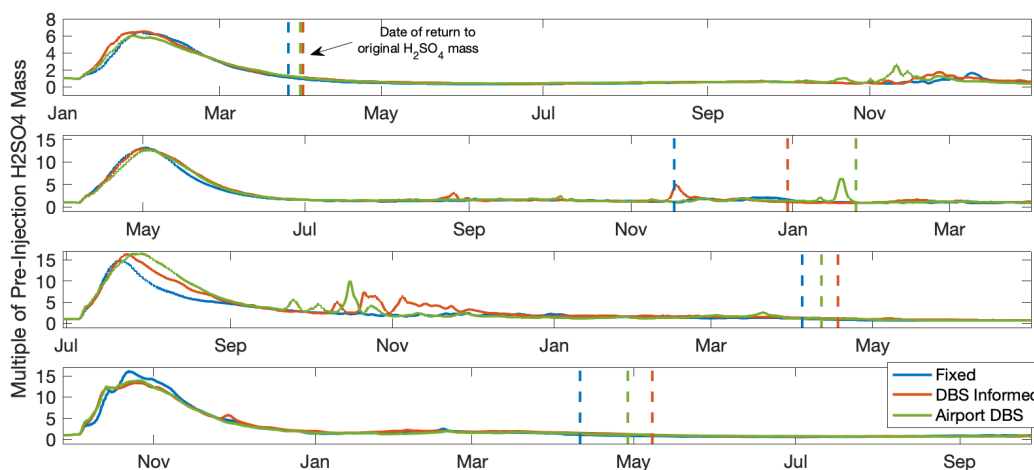
Figure 8: Calculation of H_2SO_4 mass evolution in CESM2 (WACCM6) simulations for sulfate precursor injections
305   **during four seasons. Vertical dashed lines indicate the first day at which the total mass of H_2SO_4 returned to within**
10% pre-injection values for the three injection protocols.

We also analyzed the effective global coverage of each injection protocol (Figure 8). This was calculated by projecting the
concentration of H_2SO_4 on each isentrope onto the earth's surface, and finding the fraction of the earth's surface area for which
310   the mass of H_2SO_4 was greater than the global pre-injection mean. While the short-term improvements in coverage and
distribution has been thoroughly discussed in Section 3.2, it is important to note that at yearly timescales, coverage by the
DBS-informed and airport-restricted methods was better than the fixed protocol up to 75% of the time. To put it another way,

while we identified the most important diffusive transport barriers for one week of idealized isentrope-restricted transport with no guarantees on longer behavior, the lasting presence and influence of these coherent structures is evident up to a year later.

315   Figure 10 confirms the advantages of a variable seeding method, showing that stratospheric sulfate aerosol size is generally smaller for the DBS seeding schemes than the fixed schemes. This is important because larger aerosols backscatter less (meaning more aerosol is required to achieve a given level of radiative forcing), heat the stratosphere more (resulting in greater side effects on stratospheric circulation and surface climate), and have increased sedimentation velocities (also meaning more aerosol is required) [Pierce et al., 2010; Tilmes et al., 2017; Simpson et al., 2019].
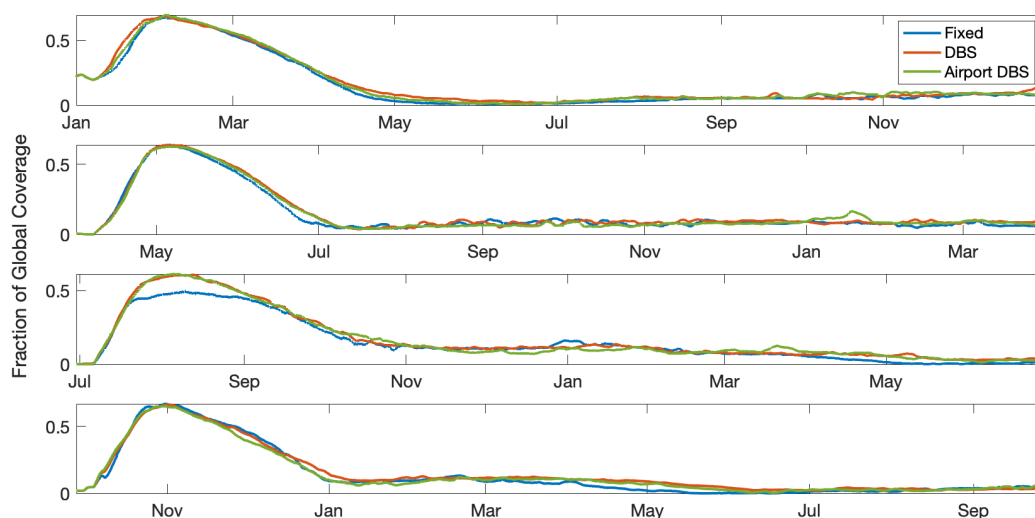
320   **Figure 9: Analysis of CESM2 (WACCM6) output showing the fraction of the earth's surface surrounded by a layer of H₂SO₄ of total mass greater than the global pre-injection mean.**
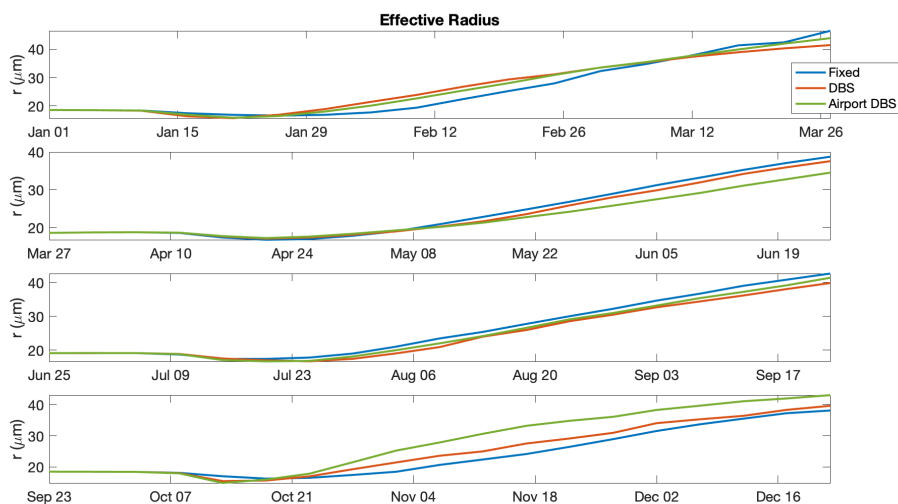
Figure 10: Effective radius of geoengineering aerosols over the first 3 months of transport along the 540K isentrope.
Note that the October injection resulted in a smaller effective radius for the fixed protocol and corresponds with the
earlier peak in global coverage in Figure 9 and the higher total mass of H₂SO₄ in Figure 8.

4 Discussion and Conclusion

Here we have explored the use of diffusive transport barriers to guide strategic injection locations for stratospheric aerosol
geoengineering. Compared to fixed-injection locations commonly used to study future climate scenarios, this dynamic
injection allows for better global coverage, often with fewer injection sites. This has important implications for previous
studies regarding the efficiency of aerosol optical depth versus injection rate; in particular, by focusing on fixed-injection
locations [e.g. Robock et al., 2008; Tilmes et al., 2017 among others], these studies appear to have underestimated the potential
coverage and therefore reflectance of geoengineered sulfate-aerosols. This finding is three-fold justified by our work. First,
with dynamic injection locations, initial particle concentrations spread much more quickly as indicated in Figures 5 and 7, thus
reducing probability of coagulation. With reduced coagulation, there will be slower descent of sulfates from the stratosphere
(and out of action), as well as increased scattering. Second, increased dispersion, as quantified by relative entropy in Figs 3 &
4, will reduce local stratospheric heating, hot spots, because heat transfer to aerosol particles in a given volume is proportional
to the mass, which is reduced by reduced concentration. Lastly, more uniform aerosol coverage, means more uniform radiative
forcing, and a more effective geoengineering protocol.

In our fully-coupled microphysics and atmospheric chemistry climate simulations, we verified that the initial improvements
in particle dispersion resulted in long-term gains even after including all the complexities of full climate model. The prolonged
presence of H₂SO₄ in the stratosphere for the two DBS-informed injection protocols speaks to a reduction in sedimentation

rates. Additionally, after many months of transport, when the atmosphere was thoroughly mixed, there was still evidence of

345 the influence of our diffusive transport barriers in the improved global coverage of H_2SO_4.

Related to this study is the proposed idea of direct injection of H_2SO_4 droplets, instead of SO_2 gas, which would ostensibly create a more monodisperse particle distribution and thus delay coagulation [Pierce et al., 2010]. The long-term advection-only analysis in Section 3.1 applies more directly to H_2SO_4 injection, in that this proposed method already injects particles, albeit with non-obvious consequences for the resulting size distribution. Further investigation is warranted to understand the

350 relative effects of this method vs the SO_2 injection simulated in our CESM2 (WACCM6) simulations, particularly if injection locations are chosen dynamically. This is especially important given the stratospheric chemistry involved in SO_2 injection, including the approximately one-month timescale of conversion from SO_2 to sulfate aerosols seen in Figures 8 and 9.

The results presented here are for a single model; different models will indicate different stratospheric features and thus different transport barrier locations and strengths. Of key importance is that the long-term dispersion analysis and structure

355 identification methodology relied on two-dimensional transport along isentropes. This method has proven to be successful for advancing the goals of optimizing sulfate precursor injections; a full three-dimensional computation of DBS fields would further improve the results. Though not investigated in the present research, with the introduction of stratospheric heating, cross-isentropic flow is likely to occur (e.g., vertical uplift from the heating), potentially justifying three-dimensional analysis of the flows used here. As this increase in complexity would exponentially increase the computational costs of finding injection

360 locations, the currently proposed isentrope method is found to be satisfactory as a benchmark improvement in injection protocols at little to no increased operational cost.

Several studies have found that the injection rate of SO_2 is the limiting factor in geoengineering efficiency by increasing coagulation [Heckendorn et al., 2009; Niemeier et al., 2011; Niemeier and Timmreck, 2015]. These studies, however, have neglected to optimize the dispersion of SO_2 during the first days following injection. This oversight has inhibited the potential

365 of sulfate injections and prevented optimal radiative forcing in model simulations. We conclude that the exploitation of readily available short-range wind forecasts and reanalysis is a catalyst that will allow better understanding of what can be achieved with climate geoengineering. While this change in injection approach does not address many of the potential hazards of geoengineering [e.g. Robock et al., 2008; Heckendorn et al., 2009], it is a significant step forward towards assessing the feasibility of geoengineering to prevent the climate from crossing a critical tipping point.

370

Author Contributions

NA, BK, DG and GH contributed to the writing of this manuscript and analysis of results. NA and GH developed the experiment design and methods. BK performed all CESM6(WACCM) model simulations. NA performed all other computations.

375

Acknowledgments

Support for B.K. was provided in part by the National Science Foundation through agreement CBET-1931641, the Indiana
380 University Environmental Resilience Institute, and the *Prepared for Environmental Change* Grand Challenge initiative. The
Pacific Northwest National Laboratory is operated for the US Department of Energy by Battelle Memorial Institute under
contract DE-AC05-76RL01830. This research was supported in part by Lilly Endowment, Inc., through its support for the
Indiana University Pervasive Technology Institute, and in part by the Indiana METACyt Initiative. The Indiana METACyt
Initiative at IU was also supported in part by Lilly Endowment, Inc. The ocean flow data used for Figures 1 and 2 can be
385 obtained from AVISO (http://www.aviso.oceanobs.com).

References

Beron-Vera, F. J., M. J. Olascoaga, M. G. Brown, and H. Koçak (2012), Zonal Jets as Meridional Transport Barriers in the
Subtropical and Polar Lower Stratosphere, *J. Atmos. Sci.*, *69*(2), 753–767, doi:10.1175/JAS-D-11-084.1.

390 BozorgMagham, A. E., and S. D. Ross (2015), Atmospheric Lagrangian coherent structures considering unresolved turbulence
and forecast uncertainty, *Commun. Nonlinear Sci. Numer. Simul.*, *22*(1–3), 964–979, doi:10.1016/j.cnsns.2014.07.011.

Crutzen, P.J. Albedo Enhancement by Stratospheric Sulfur Injections: A Contribution to Resolve a Policy Dilemma?
(2006), *Climatic Change,* 77(211), https://doi.org/10.1007/s10584-006-9101-y

Domeisen, D. I. V., Garfinkel, C. I., & Butler, A. H. (2019). The Teleconnection of El Niño Southern Oscillation to the
395 Stratosphere, *Reviews of Geophysics*, 5–47, doi.org/10.1029/2018RG000596

Driscoll, S., Bozzo, A., Gray, L. J., Robock, A., & Stenchikov, G. (2012). Coupled Model Intercomparison Project 5 (CMIP5)
simulations of climate following volcanic eruptions. *Journal of Geophysical Research Atmospheres*, *117*(17).
https://doi.org/10.1029/2012JD017607

Garaboa-Paz, D., J. Eiras-Barca, F. Huhn, and V. Peérez-Mũnuzuri (2015), Lagrangian coherent structures along atmospheric
400 rivers, *Chaos*, *25*(6), doi:10.1063/1.4919768.

Gettelman, A. et al. (2019), High Climate Sensitivity in the Community Earth System Model Version 2 (CESM2), *Geophys.
Res. Lett.*, *46*(14), 8329–8337, doi:10.1029/2019GL083978.

Global Airport Database: https://www.partow.net/miscellaneous/airportdatabase/index.html, last access: 4 May 2020.

Hadjighasem, A., and G. Haller (2016), Geodesic Transport Barriers in Jupiter's Atmosphere: A Video-Based Analysis, *SIAM
405 Rev.*, *58*(1), 69–89, doi:10.1137/140983665.

Haller, G. (2015), Lagrangian Coherent Structures, *Annu. Rev. Fluid Mech.*, 137–162, doi:10.1002/9783527639748.ch3.

Haller, G., D. Karrasch, and F. Kogelbauer (2018), Material barriers to diffusive and stochastic transport, *Proc. Natl. Acad.
Sci.*, *115*(37), 9074–9079, doi:10.1073/pnas.1720177115.

Haller, G., D. Karrasch, and F. Kogelbauer (2020), Barriers to the transport of diffusive scalars in compressible flows, *SIAM
410 J. Appl. Dyn. Syst.*, *19*(1), 85–123, doi:10.1137/19M1238666.

Harris, B. (2006), *Encyclopedia of Statistical Sciences*, 2nd, vol. ed., edited by N. Balakrishnan, C. B. Read, and B. Vidakovic, Wiley, New York.

Heckendorn, P., D. Weisenstein, S. Fueglistaler, B. P. Luo, E. Rozanov, M. Schraner, L. W. Thomason, and T. Peter (2009), The impact of geoengineering aerosols on stratospheric temperature and ozone, *Environ. Res. Lett.*, *4*(4), doi:10.1088/1748-9326/4/4/045108.

Jaiser, R., K. Dethloff, and D. Handorf (2013), Stratospheric response to arctic sea ice retreat and associated planetary wave propagation changes, *Tellus, Ser. A Dyn. Meteorol. Oceanogr.*, *65*, 1–11, doi:10.3402/tellusa.v65i0.19375.

Kashimura, H., M. Abe, S. Watanabe, T. Sekiya, D. Ji, John C. Moore, J. N. S. Cole, and B. Kravitz (2017), Shortwave radiative forcing, rapid adjustment, and feedback to the surface by sulphate geoengineering: Analysis of the Geoengineering Model Intercomparison Project G4 scenario, *Atmos. Chem. Phys.*, *18*, 3339-3356, doi:10.5194/acp-17-3339-2017.

Knutson, B., W. Tang, and P. W. Chan (2015), Lagrangian coherent structure analysis of terminal winds: Three-dimensionality, intramodel variations, and flight analyses, *Adv. Meteorol.*, *2015*, doi:10.1155/2015/816727.

Kravitz, B., D. G. MacMartin, M. J. Mills, J. H. Richter, S. Tilmes, J.-F. Lamarque, J. J. Tribbia, and F. Vitt (2017), First simulations of designing stratospheric sulfate aerosol geoengineering to meet multiple simultaneous climate objectives, *Journal of Geophysical Research*, *122*, 12616-12634, doi:10.1002/2017JD026874.

Kravitz, B. and D. G. MacMartin (2020), Uncertainty and the basis for confidence in solar geoengineering research, *Nature Reviews Earth and Environment*, *1*, 64-75, doi:10.1038/s43017-019-0004-7.

Nakamura, N. (2008), Quantifying inhomogeneous, instantaneous, irreversible transport using passive tracer field as a coordinate. *Lect Notes Phys 744*, 137-144.

Niemeier, U., H. Schmidt, and C. Timmreck (2011), The dependency of geoengineered sulfate aerosol on the emission strategy, *Atmos. Sci. Lett.*, *12*(2), 189–194, doi:10.1002/asl.304.

Niemeier, U., and C. Timmreck (2015), What is the limit of climate engineering by stratospheric injection of SO2, *Atmos. Chem. Phys.*, *15*(16), 9129–9141, doi:10.5194/acp-15-9129-2015.

Olascoaga, M. J., M. G. Brown, F. J. Beron-Vera, and H. Koçak (2012), Brief communication Stratospheric winds, transport barriers and the 2011 Arctic ozone hole, *Nonlinear Process. Geophys.*, *19*(6), 687–692, doi:10.5194/npg-19-687-2012.

Pierce, J. R., Weisenstein, D. K., Heckendorn, P., Peter, T., & Keith, D. W. (2010). Efficient formation of stratospheric aerosol for climate engineering by emission of condensible vapor from aircraft. *Geophysical Research Letters*, *37*(18), 2–6. https://doi.org/10.1029/2010GL043975

Rasch, P. J., P. J. Crutzen, and D. B. Coleman (2008), Exploring the geoengineering of climate using stratospheric sulfate aerosols: The role of particle size, *Geophys. Res. Lett.*, *35*(2), 1–6, doi:10.1029/2007GL032179.

Robock, A., L. Oman, and G. L. Stenchikov (2008), Regional climate responses to geoengineering with tropical and Arctic SO2 injections, *J. Geophys. Res. Atmos.*, *113*(16), 1–15, doi:10.1029/2008JD010050.

Rutherford, B., G. Dangelmayr, and M. T. Montgomery (2012), Lagrangian coherent structures in tropical cyclone intensification, *Atmos. Chem. Phys.*, *12*(12), 5483–5507, doi:10.5194/acp-12-5483-2012.

445   Serra, M., and G. Haller (2016), Objective eulerian coherent structures, *Chaos*, *26*(5), doi:10.1063/1.4951720.

Serra, M., P. Sathe, F. Beron-Vera, and G. Haller (2017), Uncovering the edge of the polar vortex, *J. Atmos. Sci.*, *74*(11), 3871–3885, doi:10.1175/JAS-D-17-0052.1.

Simpson, I. R., S. Tilmes, J. H. Richter, B. Kravitz, D. G. MacMartin, M. J. Mills, J. T. Fasullo, and A. G. Pendergrass (2019), The Regional Hydroclimate Response to Stratospheric Sulfate Geoengineering and the Role of Stratospheric Heating, *J.*

450   *Geophys. Res. Atmos.*, *124*(23), 12587–12616, doi:10.1029/2019JD031093.

Tallapragada, P., S. D. Ross, and D. G. Schmale (2011), Lagrangian coherent structures are associated with fluctuations in airborne microbial populations, *Chaos*, *21*(3), doi:10.1063/1.3624930.

Tang, W., M. Mathur, G. Haller, D. C. Hahn, and F. H. Ruggiero (2010), Lagrangian Coherent Structures near a Subtropical Jet Stream, *J. Atmos. Sci.*, *67*(7), 2307–2319, doi:10.1175/2010JAS3176.1.

455   The Royal Society (2009), *Geoengineering the climate: Science, Governance and Uncertainty Report*, The Royal Society, London.

Tilmes, S., R. Müller, and R. Salawitch (2008), The sensitivity of polar ozone depletion to proposed geoengineering schemes, *Science*, *320*(5880), 1201–1204, doi:10.1126/science.1153966.

Tilmes, S., J. H. Richter, M. J. Mills, B. Kravitz, D. G. MacMartin, F. Vitt, J. J. Tribbia, and J.-F. Lamarque (2017), Sensitivity

460   of aerosol distribution and climate response to stratospheric SO 2 injection locations, *J. Geophys. Res. Atmos.*, *122*(12), 12,591–12,615, doi:10.1002/2017JD026888.

Wang, N., U. Ramirez, F. Flores, and S. Datta-Barua (2017), Lagrangian coherent structures in the thermosphere: Predictive transport barriers, *Geophys. Res. Lett.*, *44*(10), 4549–4557, doi:10.1002/2017GL072568.